Mon. Not. R. Astron. Soc. **310**, 879–891 (1999)

Dynamics of the boxy elliptical galaxy NGC 1600

Michael Matthias and Ortwin Gerhard
Astronomisches Institut der Universität Basel, Venusstr. 7, CH-4102 Binningen, Switzerland

Accepted 1999 July 23. Received 1999 June 28; in original form 1998 December 30

ABSTRACT

We use three-integral models to infer the distribution function (DF) of the boxy E3–E4 galaxy NGC 1600 from surface brightness and line-profile data on the minor and major axes. We assume axisymmetry and that the mass-to-light ratio is constant in the central $\sim 1 R_e$. Stars in the resulting gravitational potential move mainly on regular orbits. We use an approximate third integral K from perturbation theory and write the DF as a sum of basis functions in the three integrals E, L_z and K. We then fit the projected moments of these basis functions to the kinematic observables and deprojected density, using a non-parametric algorithm. The deduced dynamical structure is radially anisotropic, with $\sigma_\theta/\sigma_r \approx \sigma_\phi/\sigma_r \approx 0.7$ on the major axis. Both on the minor axis and near the centre the velocity distribution is more isotropic; thus the model is flattened by equatorial radial orbits. The kinematic data are fitted without the need for a central black hole; the central mass determined previously from ground-based data therefore overestimates the actual black-hole mass. The mass-to-light ratio of the stars is $M/L_V = 6\,h_{50}$. The anisotropy structure of NGC 1600 with a radially anisotropic main body and more nearly isotropic centre is similar to that found recently in NGC 1399, 2434, 3379 and 6703, suggesting that this pattern may be common amongst massive elliptical galaxies. We discuss a possible merger origin of NGC 1600 in the light of these results.

Key words: line: profiles – galaxies: elliptical and lenticular, cD – galaxies: formation – galaxies: individual: NGC 1600 – galaxies: kinematics and dynamics.

1 INTRODUCTION

To understand the distribution of stellar orbits in elliptical galaxies is a fundamental problem in stellar dynamics. Elliptical galaxies are dynamically hot stellar systems, i.e. the velocity dispersion of the stars is generally larger than their rotational velocity. In these three-dimensional systems, the phase-space distribution function (DF) of stars must depend on classical and non-classical integrals of motion (Schwarzschild 1979), and may involve stochastic orbit building blocks (Merritt & Fridman 1996).

An important parameter for the dynamics of ellipticals is the central density slope. Parametrizing the central density as $\rho(r) \propto r^{-\gamma}$, there appear to be two groups of galaxies (Gebhardt et al. 1996): ellipticals with weak cusps ($0 \lesssim \gamma \lesssim 1.4$, peak at 0.8) and those with strong cusps ($\gamma > 1.4$, peak at 1.9). The cusp properties turn out to be related to other properties of ellipticals. Kormendy & Bender (1996) divide ellipticals into two groups:

(i) giant, cored ellipticals: non-rotating, anisotropic, boxy, moderately triaxial, with cuspy cores;

(ii) lower-luminosity power-law ellipticals: rotating, nearly isotropic, oblate-spheroidal, discy, strong cusps.

There is a range of luminosity in which both types occur. The natural question is whether these two groups have different formation histories (Faber et al. 1997).

Elliptical galaxies are generally believed to have formed by some variant of a merging process, as part of the hierarchical formation of structure in the Universe. Depending on circumstances, this could have been a multiple merger between galaxies in a group, a merger between two about-equal spiral galaxies, or a merger between a dominant galaxy and several minor companions. Numerical simulations of such merging processes have been published, e.g. by Weil & Hernquist (1996), Barnes & Hernquist (1996) and Dubinski (1998), respectively.

The shape and dynamical structure of the final remnant elliptical galaxy depends sensitively on the influence of the dissipational component during the collapse (Barnes & Hernquist 1996). Even a small fraction of the mass in gas is sufficient to drive the evolution towards axisymmetry: in these calculations, including 10 per cent of the mass of the discs in the form of gas changed a near-prolate final remnant with axis ratios 10:5:4 to a near-oblate one with axis ratios 10:9:6. The remnants of dissipationless mergers are also expected to evolve slowly towards axisymmetry (Merritt & Quinlan 1998), driven by their central supermassive black holes: most spheroidal galaxies are now believed to contain a central black hole with a fraction of $\lesssim 0.5$ per

cent of the spheroid mass (Richstone et al. 1998; Magorrian et al. 1998). In both cases, the mechanism responsible appears to be the destabilization of the box orbits by the deep potential well, first studied by Gerhard & Binney (1985). The evolution caused by the black hole proceeds through a sequence of quasi-equilibria by stochastic diffusion (Merritt & Fridman 1996).

These theoretical expectations are consistent with the results of Franx, Illingworth & de Zeeuw (1991), who used observations of minor axis rotation to show that most ellipticals are likely to be near-axisymmetric, with the majority of near-oblate shape and a smaller fraction of near-prolate shape. However, the distribution of apparent axis ratios of the giant cored ellipticals is inconsistent with their being precisely axisymmetric (Tremblay & Merritt 1996). The majority of ellipticals without significant minor axis rotation, including NGC 1600, are thus likely to be near-oblate triaxial objects.

While quantitative information about the expected internal kinematics and phase-space structure of evolved merger remnants is still scarce, it is clear that comparing this with the orbit distributions inferred from observations will give important constraints on the processes that shape ellipticals. We have therefore started a project to determine the stellar distribution functions (DFs) of flattened elliptical galaxies from kinematic data.

An essential part of our technique is the use of an approximate third integral of motion. Based on the results discussed above, we approximate the mass distribution and potential as axisymmetric. We calculate an effective third integral of motion for the regular regions of phase space (after Gerhard & Saha 1991), and then seek a distribution function over three integrals that matches a given set of photometric and kinematic data. The method used to determine the DF is non-parametric and includes regularization of the DF. In this paper we describe the technique and, as a first case, analyse the surface brightness, velocity dispersion and line-profile data for the non-rotating E3–E4 galaxy NGC 1600. It is known that some ellipticals, especially NGC 1600, cannot be fitted by two-integral models (Binney, Davies & Illingworth 1990; van der Marel 1991).

The paper is organized as follows. In Section 2 we briefly summarize the observational data, and discuss our assumptions in Section 3. Our technique to infer the DF is explained in detail in Section 4. The results for NGC 1600 and a discussion follow in Sections 5 and 6, respectively.

2 OBSERVATIONAL DATA

NGC 1600 is a bright ($M_B = -23.17$) elliptical galaxy at a distance of $D = 93\,\mathrm{Mpc}$ (for $H_0 = 50\,\mathrm{km\,s^{-1}\,Mpc^{-1}}$). To derive the stellar density distribution we have used surface photometry of NGC 1600 from Bender (private communication). The effective radius is $R_\mathrm{e} = 48\,\mathrm{arcsec}$ ($21.6\,h_{50}^{-1}\,\mathrm{kpc}^{-1}$). To constrain the dynamical models, we have used velocity dispersions and line-profile shape parameters measured by Bender, Saglia & Gerhard (1994). Older velocity dispersion data by Jedrzejewski & Schechter (1989) do not contain line-profile shape information and show systematically lower velocity dispersions in the region of overlap, especially in the centre. We have therefore decided to use only the newer data by Bender et al. (1994) in the modelling. These data extend to approximately $R_\mathrm{e}/2$ along both the major and minor axes; the data are binned to eight points on the major axis and eleven on the minor axis. The line-profile shapes are expanded in Gauss–Hermite moments.

NGC 1600 shows only little rotation. The maximal rotation velocity is around $30\,\mathrm{km\,s^{-1}}$ but most of the measured rotational velocities are below $20\,\mathrm{km\,s^{-1}}$ with errors of comparable size. Consistent with the lack of rotation, the skewness of the line profiles is nearly zero, except at one radius where $h_3 \approx -0.15$. In the following, we therefore use only the σ and h_4 data.

3 ASSUMPTIONS

As discussed in the Introduction, both theory and observation suggest that old giant ellipticals are triaxial but not far from axisymmetric. The small measured rotation velocities and h_3 parameters on the minor axis then suggest that NGC 1600 is near-oblate. Therefore we assume an oblate-axisymmetric mass distribution and potential. This assumption is undoubtedly only an approximation – the results of Hunter & de Zeeuw (1992) indicate that we should expect about 20 per cent of the total mass of stars on box-like and x-tube orbits if NGC 1600 is triaxial with axis ratios $\sim 10 : 9 : 6$ – but it makes the subsequent analysis much easier and is likely to give approximately correct kinematic results. We will see whether the data for NGC 1600 can be fitted by an axisymmetric model or whether triaxiality is required by the kinematics.

The projected axis ratio of NGC 1600 is E3–E4. Intrinsically flatter-cored ellipticals are rare (Tremblay & Merritt 1996), thus NGC 1600 is likely to be nearly edge-on. We therefore assume an inclination angle of exactly $i = 90°$; this ensures that the deprojection of the surface density is unique. If the geometry is not edge-on, disc-like konus densities can be added to the density without altering the surface brightness (Gerhard & Binney 1996); however, the resulting uncertainty in the three-dimensional density distribution decreases to zero as $i \to 90°$.

The small measured rotation velocities and h_3 parameters on the major axis of NGC 1600 are consistent with the assumption that this galaxy is non-rotating. In this case, the skewness (and all higher odd Gauss–Hermite moments) of the line profiles vanish and we remain with the velocity dispersion and h_4 kinematical data. Non-rotating models have DFs even in L_z, so that we restrict ourselves to models even in L_z.

Finally, we assume a constant (but free) mass-to-light ratio M/L in the central $R_\mathrm{e}/2$, where we have kinematical data, i.e. we assume that in this region the high density of stars dominates over the dark-matter density. This assumption appears reasonable in view of the low central $M/L_B = 3.3$ inferred for the E0 galaxy NGC 6703 even when the stars have the maximum mass compatible with the central kinematics (Gerhard et al. 1998). In this galaxy, the dark halo does not become important until $\approx 1 R_\mathrm{e}$.

4 THE METHOD

Our aim is to obtain a three-integral distribution function for NGC 1600 by modelling all data (surface brightness and line profiles on two axes) simultaneously in a χ^2-sense. Because the third integral is calculated from the perturbation away from a spherical *potential*, we derive in a first independent step the three-dimensional density distribution from the observed surface brightness and then the gravitational potential from the density. Under the assumptions made we obtain a unique $\rho(R, z)$ and $\Phi(R, z)$. Given the potential, the approximate third integral is a series expansion in the action-angle variables of the spherical part of $\Phi(R, z)$ (see Gerhard & Saha 1991).

We then set up basis functions for the DF that depend on the three integrals E, L_z and the third integral K. For each basis

function we calculate moments that are projected along the line of sight. The DF is written as a sum over these basis functions and its projected moments are linear sums over the corresponding moments for the basis functions. The coefficients are determined by fitting directly to the observations, except for the model densities, which are fitted to the already deprojected $\rho(R,z)$.

The determination of the DF from observations by this process is an ill-posed problem (see, e.g., Merritt 1993), because the observables are integral moments of the underlying DF, and so small changes in the observables lead to large changes in the recovered DF (spikes). Typically, the inferred function becomes spiky because of the amplification of structures induced by measurement errors. To avoid this, we include a regularization term in the χ^2-function; this is minimized by a linear fitting routine within the usual non-negativity constraints and mass conservation. In this way, a smooth DF consistent with the data is found.

Our approach of analyzing line-profile data for axisymmetric galaxies is related to that of van der Marel et al. (1998), Gebhardt et al. (1999) and Cretton et al. (1999), who use a generalized version of Schwarzschild's method, and to that of Dejonghe et al. (1996) and Emsellem, Dejonghe & Bacon (1999), who use a Stäckel integral obtained from fitting a single Stäckel potential to the potential of the galaxy under study. The difference is that we use a third integral derived from the galaxy potential rather than following individual orbits, and that we take care to investigate how well our third integral actually represents the orbits in this potential. In the following, we describe the different steps in our method and their application to NGC 1600 in more detail.

4.1 Deprojection and gravitational potential

With the above assumptions the deprojection is unique and the gravitational potential is determined by the density up to a constant factor. We used a program by Dehnen (1995) that calculates the density $\rho(R,z)$ from the surface brightness $\Sigma(X,Y)$ by a Lucy-algorithm (Lucy 1974), and then evaluates the potential $\Phi(R,z)$ for constant M/L ratio as a sum of spherical harmonics. Here (X,Y) are sky-coordinates and (R,z) are coordinates in the meridional plane of the galaxy. Between Lucy steps the density is smoothed using FFT filtering.

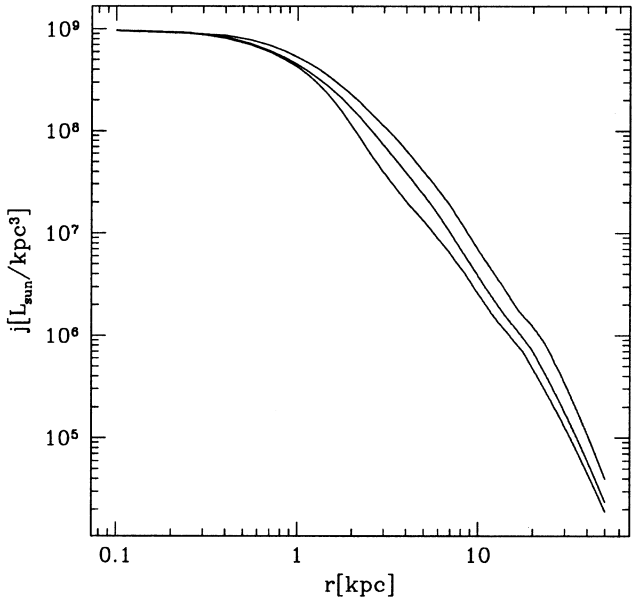

Figure 1. Three-dimensional luminosity density of NGC 1600 along the minor, major and an intermediate axis, from deprojecting the observed surface brightness distribution with $i = 90°$.

The calculation is done on a grid where the grid points lie on 11 rays through the $(R \geqslant 0,\ z \geqslant 0)$ quadrant of the meridional plane, including the two axes. The grid extends to a maximum radius of 30 kpc. For NGC 1600, the density is thus extrapolated slightly beyond the edge of the CCD data (corresponding to a galactocentric radius of 28 kpc). The extrapolation assumes a power-law with exponent $\gamma = -4$ at large radii.

Fig. 1 shows density profiles along three axes resulting from this deprojection. The deprojected central density slope is $\gamma = 0.24$, consistent with the result found by Gebhardt et al. (1996). NGC 1600 is the only galaxy in their sample that is consistent with a flat central density profile. The mean axial ratio of the deprojected density distribution in Fig. 1 is $c/a = 0.68$.

4.2 Third integral

In an axisymmetric potential, the classical integrals of motion are the energy E and the z-component of the angular momentum L_z. Numerical orbit integrations show, however, that particles in the potential of NGC 1600 obey an approximate third integral of motion (see below), which we call K. Gerhard & Saha (1991) developed a method to calculate an approximation for the third integral. This is based on resonant perturbation theory and uses a Lie-transform of the unperturbed integrals in terms of the action-angle variables of the unperturbed spherical part of the potential. The expression obtained for the third integral is usually a good approximation if the density is rounder than $c/a \simeq 0.5$. Dynamical models making use of this third integral were studied by Dehnen & Gerhard (1993a,b) for a perturbed isochrone sphere.

Here the algorithm has been generalized for the potentials of real galaxies. The deprojected density distribution of the galaxy is expanded in spherical harmonics and the corresponding gravitational potential is derived. As unperturbed integrable potential we take the spherical part of this potential expansion, and for the perturbation we here take the $l = 2$- and $l = 4$-terms, but excluding a 4:3 resonance term. The resulting resonant invariant describes the 2:1 resonant (in terms of the frequencies of the spherical system) meridional butterfly orbits, and is of sufficient accuracy to describe most z-tube orbits well. We make no attempt to treat the 4:3 and other resonant orbit families specially; by using our resonant invariant we effectively fitted a tube orbit torus through each chain of resonant islands.

Fig. 2 illustrates this by showing two typical surfaces of section for the potential of NGC 1600, calculated by numerically solving the equations of motion. Overlayed are the contours of K calculated by perturbation theory at values of K corresponding to the mean values of K along each orbit. The top panel shows zero-angular-momentum orbits at an energy corresponding to a circular orbit radius of $R_c = 2$ kpc. The agreement is excellent; the error of the third integral along an orbit is typically two per cent. A corresponding $L_z = 0$ surface of section at $R_c = 10$ kpc looks similar: there are still almost no stochastic orbits and the description of the invariant curves by the third integral K is similarly good. The bottom panel of Fig. 2 shows higher-angular-momentum orbits $[L/L_{\rm circ}(E) = 0.4]$ at an energy corresponding to $R_c = 10$ kpc. There are now some significant families of

resonant islands that are not fitted by the resonant invariant as used here, but are approximated by tube orbit tori.

For a steady-state galaxy the strong Jeans theorem states that the distribution function f of the stars depends on the three independent integrals of motion only, provided all stars move on regular orbits with incommensurable frequencies (Binney & Tremaine 1987). For NGC 1600 this is nearly the case as Fig. 2 shows. Therefore we now seek a function $f(E, L_z, K)$ that can reproduce all available observations for NGC 1600, i.e. surface density, velocity dispersion and line-profile shapes.

4.3 Integral space

The classical integrals E and L_z together with the third integral K form a complete set of coordinates for the integral space (Dehnen & Gerhard 1993a). In integrable potentials, where the third integral is conserved exactly, each point of the integral space represents a single orbital torus. In the present case, where the third integral is only an approximation, albeit a good one (Fig. 2), this is nearly true.

For fixed energy, the integral space has a triangular shape, defined by the range of values taken by the two other invariants L_z and K. In the representation shown in Fig. 3, L_z is normalized by the angular momentum of the circular orbit in the equatorial plane. In the plots in Fig. 3, the equatorial circular orbit is thus located at $L_z/L_{\rm circ} = 1$ in the right-hand corner. The adjacent boundary at high values of K delineates equatorial orbits with radial action increasing to the left, the boundary at low values of K represents shell orbits with vertical excursions increasing towards the lower left. Orbits with $L_z = 0$ can be separated into two groups, depending on their values of K. Those with K less than a critical value $K_{\rm crit}$, indicated by the square on the left boundary, are meridional loop orbits, those above the critical value are meridional butterflies that shrink vertically as the equatorial radial orbit is approached in the upper left-hand corner.

Using the value of $K_{\rm crit}$, shape invariants S_r, S_m can be constructed from L_z, K such that they describe the radial and meridional extent of the orbits (these are approximate turning point variables; see Dehnen & Gerhard 1993a,b). The critical value $K_{\rm crit}$ depends on energy; below a certain energy $K_{\rm crit}$ is identical with $K_{\rm min}(0)$, the minimum value of K at $L_z = 0$. In this case the contours of S_m cluster at $K_{\rm min}(0)$ and the area covered by each 'box' between contour lines in Fig. 3 vanishes. In addition, the shape invariants become singular at the critical $K_{\rm crit}$, i.e. their derivatives with respect to L_z and K are indefinite at this point (Fig. 4). Because we need a smooth representation of the integral space and a smooth and differentiable phase-space distribution function f, we have therefore constructed a new representation of integral space.

To this end we introduce a new quantity

$$K_s = 1 - \frac{K_{\rm max}(L_z) - K}{K_{\rm max}(0) - K_{\rm min}(0)}. \quad (1)$$

Contours of K_s are contours of scaled $K_{\rm max}(L_z) - K$: the upper boundary is shifted downwards according to the value of K. Fig. 5 shows contours of the new set of invariants L_z and K_s on several energy surfaces through integral space. On the upper boundary line in these diagrams equatorial orbits have $K_s = 1$, and for the closed meridional loop in the lower left-hand corner of integral space $K_s = 0$. Now the area covered by each box between contour lines is approximately constant and no singularities appear. In the following we use the invariants E, L_z and K_s as a representation of integral space.

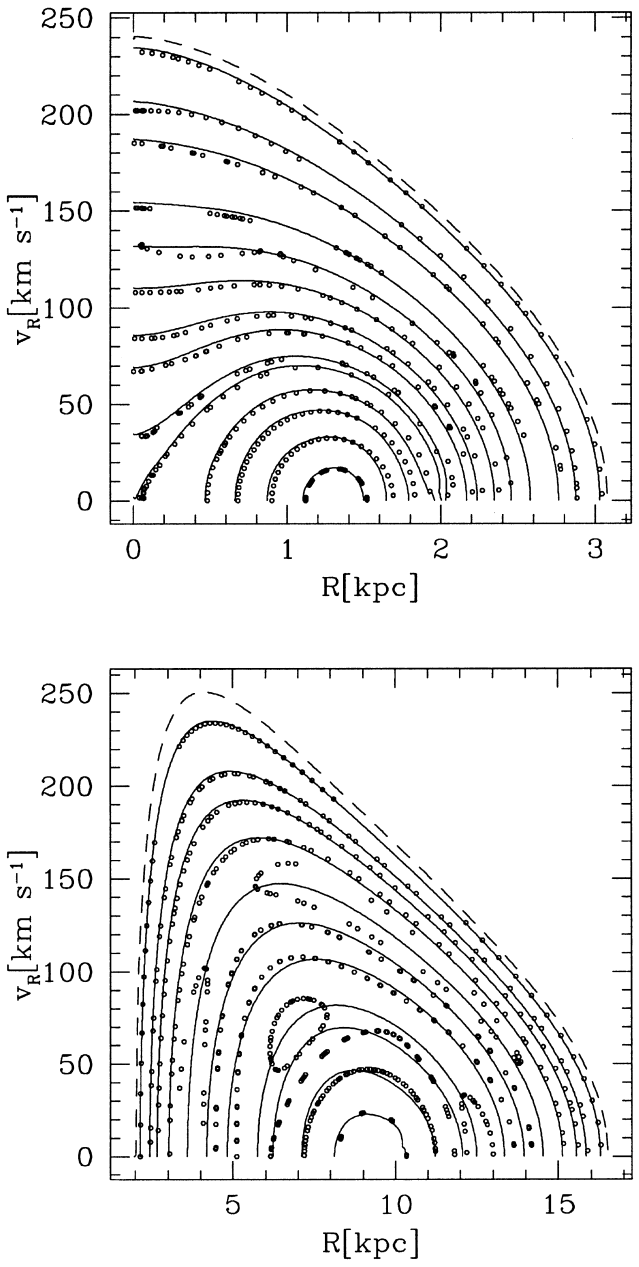

Figure 2. Top: A typical surface of section for $L_z = 0$ orbits in NGC 1600. The squares represent numerically integrated orbits, whereas the overlayed lines are contours of constant third integral K. The energy for this SOS was chosen so that the radius of the circular orbit in the equatorial plane is $R_{\rm c} = 2\,{\rm kpc}$. Bottom: high-energy SOS with $L_z/L_{\rm circ}(E) = 0.4$; here $R_{\rm c} = 10\,{\rm kpc}$.

4.4 Distribution function

The DF is written as a sum over basis functions $f_l(E, L_z, K_s)$:

$$f(E, L_z, K_s) = \sum_{l=1}^{l_{\rm max}} \alpha_l f_l(E, L_z, K_s). \quad (2)$$

Suitable basis functions are constructed using the separation ansatz

$$f_l(E, L_z, K_s) = f_{ij}(E, L_z, K_s) = g_i(E) \times h_j(L_z, K_s). \quad (3)$$

The functions $g_i(E)$ describing the energy dependence of the DF

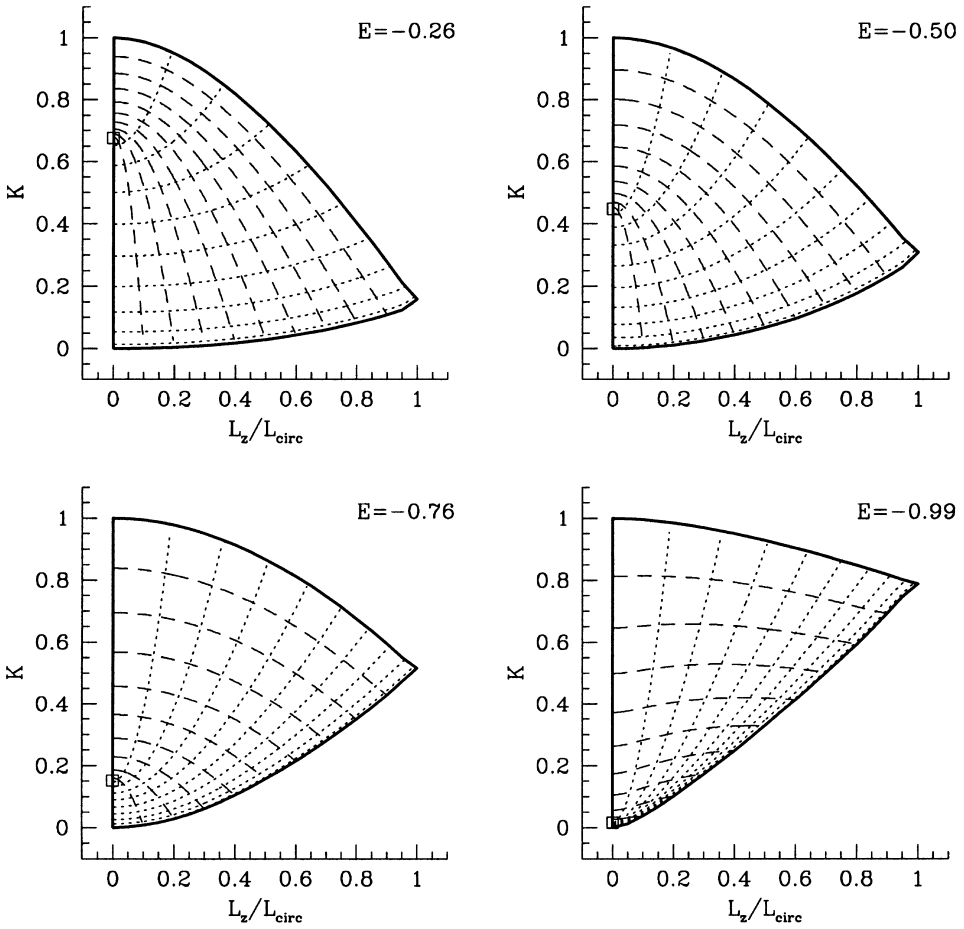

Figure 3. Integral space for four different energies ranging from $E = -0.26$ (top left) to $E = -0.99$ (bottom right). The circular orbit radii corresponding to these energies are $R_c = 16, 6, 2.2, 0.5$ kpc. In these diagrams the circular orbit in the equatorial plane is at the right-hand corner, the equatorial radial orbit at the top left, and the closed meridional loop orbit at the lower left corner. Equatorial orbits lie on the upper right boundary, shell orbits on the lower right boundary, meridional butterfly orbits on the upper part and meridional loop orbits on the lower part of the left-hand boundary. The box on the $L_z = 0$ axis denotes the critical orbit at K_{crit} dividing the latter two families. The dotted lines represent the shape invariant S_r, the dashed lines S_m. Note the crowding of contour lines near K_{crit}.

are determined as follows. First, we construct an isotropic DF $f_{iso}(E)$ whose zeroth moment approximates the spherically averaged density profile of the galaxy. This function is used as the basic energy function; further energy functions are constructed by multiplying this isotropic function by binomials centred at different energies E_i. The E_i are chosen such that the corresponding $g_i(E)$ probe different regions in energy and cover the total energy range approximately uniformly. In this paper, we use seven energy basis functions $g_i(E)$.

The basis functions $h_j(L_z, K_s)$ that describe the orbit distribution on energy surfaces are constructed using powers of the (new) invariants $|L_z|^m K_s^n$ with $n + m \leqslant 4$. These 15 angular basis functions plus two additional isotropic components ($\propto E$ and E^2), are multiplied by all of the energy basis functions, giving a set of $l_{max} = 7 \times (15 + 2) = 119$ basis functions $f_l(E, L_z, K_s)$. The DF is a linear combination of these f_l with weights α_l; cf. equation (2).

4.5 Velocity space and line-of-sight integration

All observables are line-of-sight projections of the intrinsic quantities, e.g. the surface brightness $\Sigma(X, Y)$ at a point (X, Y) on the sky is given by $\Sigma(X, Y) = \int_{-\infty}^{\infty} \mathrm{d}Z\, \rho(X, Y, Z)$, where Z is the coordinate along the line of sight and $\rho(X, Y, Z)$ the intrinsic density at (X, Y, Z). This itself is an integral over velocity space: $\rho(X, Y, Z) = \int_{-\infty}^{\infty} \mathrm{d}^3 v f(\boldsymbol{r}, \boldsymbol{v})$, with $\boldsymbol{r} = (X, Y, Z)$ and $f(E, L_z, K_s)$ the distribution function. Thus we may write $\Sigma = \mathbf{S}f$, where the operator $\mathbf{S} \equiv \int_{-\infty}^{\infty} \mathrm{d}Z\, \mathrm{d}^3 v$. The same operator is needed to calculate the projected velocity dispersion and Gauss–Hermite moments from the DF. Here we describe the evaluation of the velocity and line-of-sight integrals.

We perform the integrations over velocity space in the manner of Dehnen & Gerhard (1993a). Using axisymmetry, and after a transformation of the integration variables ($\mathrm{d}^3 v \rightarrow \mathrm{d}E\, \mathrm{d}L\, \mathrm{d}L_z$), the operator $\mathbf{R} \equiv \int_{-\infty}^{\infty} \mathrm{d}^3 v$ becomes

$$\mathbf{R} \equiv \int_{-\infty}^{\infty} \mathrm{d}^3 v|_{R,z} = \frac{1}{r} \int_{\Phi(R,z)}^{E_{max}} \mathrm{d}E \int_0^{r\sqrt{2[E-\Phi(R,z)]}} \times \frac{L\, \mathrm{d}L}{\sqrt{2[E - \Phi(R, z)]r^2 - L^2}} \times \int_{-RL_r}^{RL/r} \frac{\mathrm{d}L_z}{\sqrt{(RL/r)^2 - L_z^2}} \sum_{\substack{sgn(\dot{r})=\pm \\ sgn(\dot{\theta})=\pm}} . \quad (4)$$

As usual, R and z are cylindrical coordinates, $r^2 = R^2 + z^2$, and $\Phi(R, z)$ is the gravitational potential in the meridional plane. The

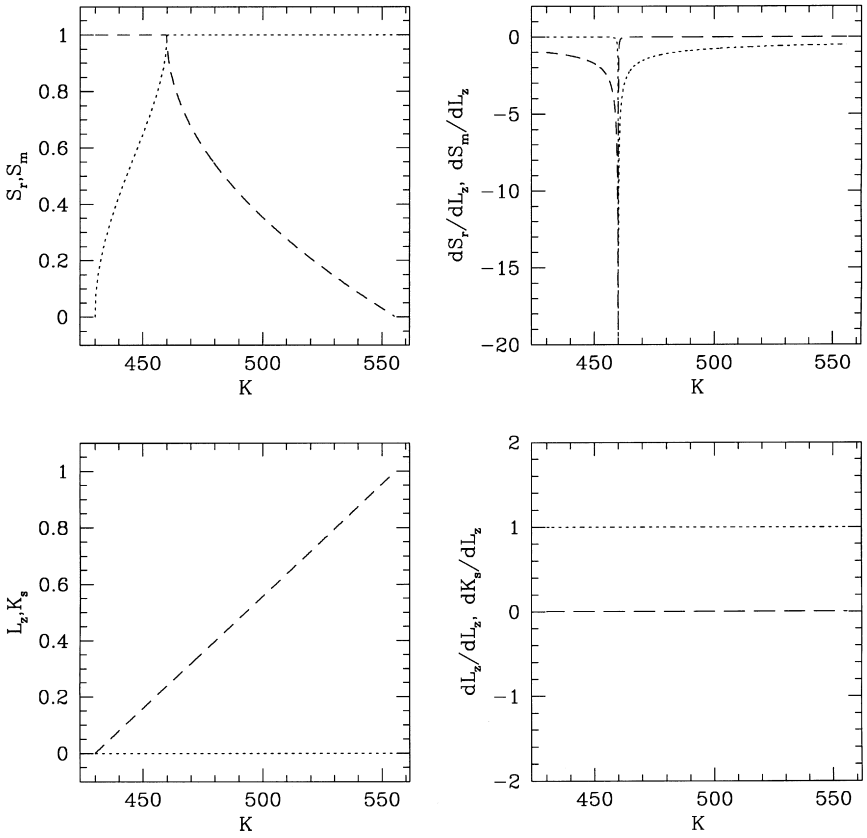

Figure 4. Old (top panels) and new invariants (bottom panels) on the $L_z = 0$ axis for some fixed energy. The left column shows the invariants and the right column the derivatives with respect to L_z and K. Clearly visible is the singular behaviour of the old invariants at $K = K_{\rm crit}$, which the new invariants L_z and K_s do not show.

maximal energy $E_{\rm max}$ appearing as the upper integration boundary should be the value of the gravitational potential at infinity, but in practice we use the value of the potential at a distance of 30 kpc along the major axis (see Section 4.1).

The operator **R** is applied to functions of velocity (depending on the desired moment) times the basis functions $f_{\mathcal{E}}(E, L_z, K_s)$ that involve the third integral K. Because the computation of K is time consuming, values of K are pre-calculated on a grid in E, L and L_z for each point of the grid in the meridional plane. Thus the integrand can be evaluated only on the grid points, and we have therefore performed the integrations over L_z and L by Gauss–Tschebyschev- and Gauss-quadrature, respectively. For the remaining integral over energy, we use spline interpolation and a Bulirsch–Stoer integrator.

The velocity integration yields the intrinsic moments, such as the density and velocity dispersions, in the meridional plane of the galaxy. These are integrated along the line of sight to obtain the observable moments. For this we also use a Bulirsch–Stoer integrator and interpolate bilinearly in the meridional plane for the minor axis kinematic data, and in the equatorial plane for the major axis data.

4.6 The fitted velocity moments

Having obtained the intrinsic and projected moments of all basis functions, the DF for a galaxy can now be found by matching to the observed moments. The quantities included in the fit are the density, the velocity dispersions on the major and minor axes, and the measured line-profile parameters (h_4 in the case of NGC 1600, and possibly h_3 and higher h_n). Some details are described in this subsection.

(i) Density: the model is required to fit the deprojected three-dimensional brightness distribution

$$\rho(R_i, z_i) = \sum_l \rho_l(R_i, z_i) \tag{5}$$

on a grid (R_i, z_i) in the meridional plane, with $\rho_l(R_i, z_i) = \mathbf{R} f_l(E, L_z, K_s)$. The employed grid is similar to that used in the deprojection in that the grid points lie on 11 rays through the $(R \geqslant 0,\ z \geqslant 0)$ quadrant of the meridional plane, including the two axes. This grid extends to a maximum radius of 26.6 kpc. The large range in radius allows us to estimate the contribution of high-energy stars on near-radial orbits to the kinematic moments further in.

(ii) Velocity dispersion: the velocity dispersion given by Bender et al. (1994) is *not* the second moment of the DF σ_0, but corresponds to the parameter $\sigma_{\rm fit}$ in a several-parameter fitting function for the entire line profile, including the h_3 and h_4 terms. Only when $h_3 = h_4 = 0$ will σ_0 be equal to $\sigma_{\rm fit}$. Thus we first determine the second moments of the observed line profiles by integrating over the line profile $l(v_\parallel)$ as specified by ($\sigma_{\rm fit}$, $v = 0$, $h_3 = 0$, h_4). For negative h_4, we integrate only up to the velocity where $l(v_\parallel)$ first becomes negative. Setting $v = h_3 = 0$ assumes that rotation is negligible.

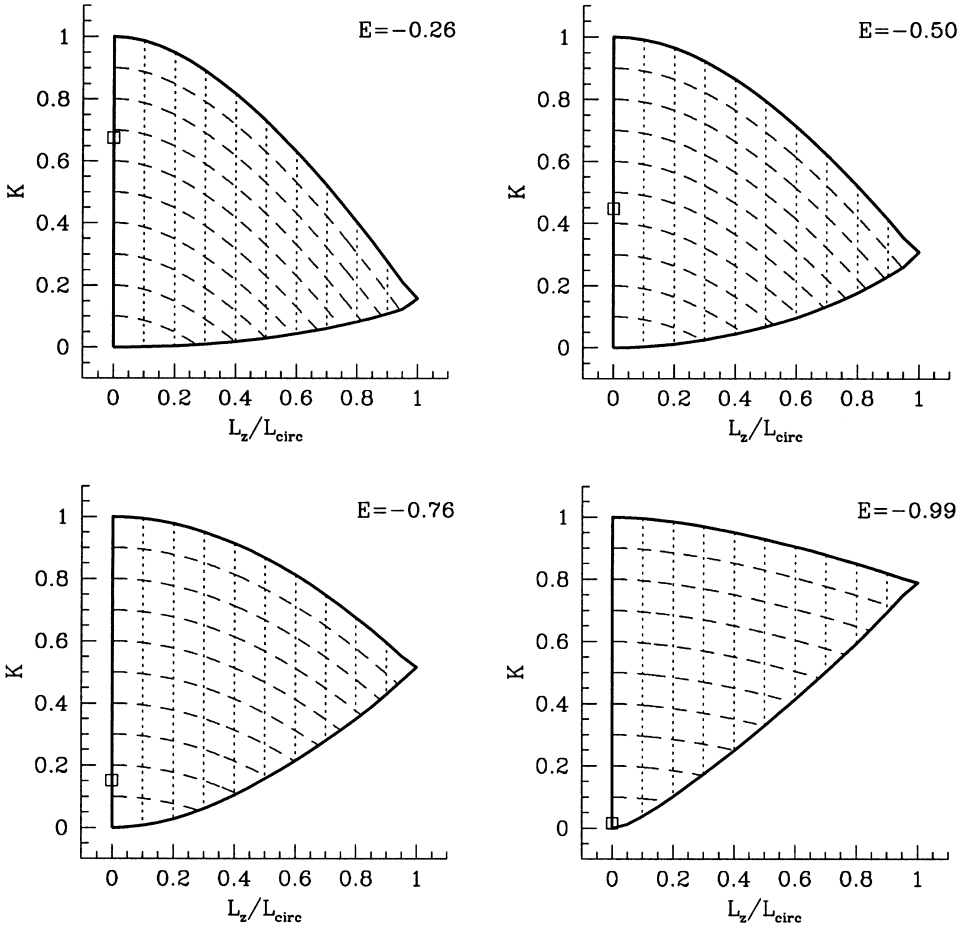

Figure 5. Same as Fig. 3 but for the new invariants L_z and K_s; see text. Now the integral space is divided by the contours into regular cells and the crowding of contours near the critical orbit has disappeared.

Given estimates for σ_0, the model is required to satisfy

$$\Sigma\sigma_0^2 = \sum_l \alpha_l \Sigma_l \sigma_{ll}^2 \tag{6}$$

at the positions of all data points. Here σ_{ll} is the projected velocity dispersion of the basis function l, Σ_l its surface brightness, and the total surface brightness $\Sigma = \sum_l \alpha_l \Sigma_l$ from equation (5).

(iii) Gauss–Hermite parameter h_4: the measured line-profile parameters h_4 depend nonlinearly on the galaxy's DF and can therefore not directly be used in a linear least squares algorithm. We therefore transform to a new set of even Gauss–Hermite moments $s_n^{(\hat{v},\hat{\sigma})}$, using fixed fiducial velocity scales $\hat{v}(X_i, Y_i)$ and $\hat{\sigma}(X_i, Y_i)$, where (X_i, Y_i) denote the position of the ith data point on the sky plane. These fiducial velocities are taken from a dynamical model that approximately matches the observed velocity dispersions and has $\hat{v}(X_i, Y_i) = 0$. This ensures that the transformed Gauss–Hermite series converge quickly.

Expressed in terms of the new s-moments, the observed line-profile shapes now depend linearly on the DF:

$$\Sigma s_n^{(\hat{v},\hat{\sigma})} = \sum_l \alpha_l \Sigma_l s_{n,l}^{(\hat{v},\hat{\sigma})} \tag{7}$$

with $s_{n,l}^{(\hat{v},\hat{\sigma})}$ the Gauss–Hermite moments of the lth basis function evaluated with the same velocity scales $(\hat{v}, \hat{\sigma})$. We have calculated and required the model to match s-moments up to order s_6.

4.7 Linear χ^2 fitting including regularization

The constraint equations (5)–(7) involve the integral operators **R** and **S**. Inferring the DF by solving these equations is an ill-posed problem in the sense that small changes in the observational data can lead to large variations in the inferred function. To prevent artificial spiky structures in the inferred DF generated by noise in the data, one has two principal possibilities (e.g. Scott 1992; Merritt & Tremblay 1994). One is to try a *parametric* inversion, i.e. fitting a function $f_p(r|a, b, c, \ldots)$ with a small number of parameters $a, b, c, \ldots$ The resulting f_p is always smooth, but because the fixed functional form of f_p may not be suitable for the true function $f(r)$, features may be induced that are not real (bias).

The other is to use a *non-parametric* inversion, where the inferred function is represented by a large number of elements α_i (values on grid points, basis functions, etc.) that give $f_{\rm np}(r|\alpha_i)$ the freedom to match any function f. Such an inversion must be regularized, for otherwise the fit to the data will be too good (χ^2 per point <1) and the resulting $f_{\rm np}(r|\alpha_i)$ will contain unphysical structure that depends purely on the noise in the data. A common method is to restrict the curvature or second derivative of the inferred function (Wahba & Wendelberger 1980). Instead of the usual χ^2-function, one minimizes the quantity

$$\xi^2 = \chi^2 + \lambda P(f) = \frac{1}{n}\sum_j \frac{[O_j - O(r_j)]^2}{\sigma_j^2} + \lambda \int_0^\infty {\rm d}r [f''(r|\alpha_i)]^2, \tag{8}$$

where O_j denotes the jth measurement at position r_j with error σ_j. $O(r_j)$ represents a linear operator that relates the function space to the observable space; in our case this will be **R** and **S**. The fitting of the data is done in the space of the observations, whereas the regularization happens in the intrinsic space of the DF. The parameter λ determines the amount of regularization: for $\lambda = 0$ the standard χ^2 fitting is recovered, for $\lambda = \infty$ the result is determined by the regularization function. In the case given, one obtains a linear function whose slope and offset are determined by the data. In astronomical applications, the data often do not sample the desired functions very well. Then it is necessary to use relatively large values of λ, and so the result will again be somewhat biased, by the form of the regularization term.

We have chosen the second approach as the one that will adapt more easily to future large and accurate kinematic data sets. We use basis functions rather than grid cells in integral space because, owing to the complexity of the third integral K_s, the complicated phase-space boundaries of such grid cells make it difficult to apply the operators **R** and **S**. The number of basis functions is adapted to the NGC 1600 data, but this is easy to change.

Because all projected moments depend linearly on the DF, we use the constrained linear least squares NETLIB routine *lfit* (Hanson & Haskell 1981), which solves, in a χ^2 sense, a set of equations $\boldsymbol{y} = \mathbf{A}\boldsymbol{x} + \boldsymbol{b}$, subject to linear equality ($\boldsymbol{y} = \mathbf{E}\boldsymbol{x} + \boldsymbol{c}$) and inequality constraints $\boldsymbol{y} \leqslant \mathbf{U}\boldsymbol{x} + \boldsymbol{d}$. In our case, the matrix **A** consists of equations for the density, the velocity dispersion, the first three even s-moments and the regularization terms. The latter can be included in the linear fitting routine because the penalty function $P(f)$ has a quadratic form; in practice we ask the routine to solve $f'' = 0$ on a grid in integral space, again in a χ^2 sense and suitably weighted by 'errors' $\lambda^{-1/2}$. For the employed grid, this gives rise to 5184 additional linear equations.

The only equality constraint we have included in the matrix **E** is a luminosity (or mass) conservation constraint. The need for this arises because of the smoothing term and because the density is fitted only in a χ^2-sense. For fixed λ, the model's penalty function $P(f)$ can be reduced by either decreasing the curvature of the model or by multiplying all basis functions $f_l(E, S_r, S_m)$ by a fixed number less than one. Depending on the shape of the ξ^2 hypersurface, it is possible that scaling of the model is favoured over reducing the curvature. To ensure that the total brightness of the model remains equal to that of the galaxy, we add an equality constraint that forces the solution to have the same total luminosity as the observed galaxy.

Finally, the non-negativity of the DF is imposed on a grid of 10920 points in E, K and L_z and defines the components of matrix **U**.

The weights for the several fitted quantities are determined as follows: for the relative weights of the dispersion and s-moments, we use the values of Gerhard et al. (1998) determined by Monte Carlo simulations. Minor and major axis kinematic data have the same weights. The relative weights of the density and kinematics were chosen in such a way that the overall rms error in the density was less than 1 per cent. The final free parameter is the smoothing parameter λ, which we have chosen such that the solution is sufficiently smooth but still fits the kinematical data well.

4.8 Monte Carlo tests

We have tested our method with artificial data, as follows: we choose a DF $f^{\rm MC}(E, L_z, K)$, constructed by fitting the deprojected density and kinematics of NGC 1600 with a set of basis functions different from those used in the normal fitting procedure so as to test the ability of our basis to reproduce general distribution functions. We calculate the projected kinematics of $f^{\rm MC}(E, L_z, K)$ and then draw artificial data points from the model kinematics at the positions of the observed data points and with their respective errors. We save $f^{\rm MC}$ on a grid in E, L_z and K for later comparision with the DF inferred from the artificial data.

Using the scheme described above we then obtain a solution for a DF, now fitting the density and the artificial kinematic data with our normal basis. A χ^2 measure of the deviation in the DF is

$$\chi^2 = \frac{1}{N_{\rm g}} \sum_{i=1}^{N_{\rm g}} \left(\frac{f_{\rm i} - f_{\rm i}^{\rm MC}}{f_{\rm i}^{\rm MC}} \right)^2 ,$$

where $N_{\rm g}$ is the number of points of the grid in integral space, $f_{\rm i}$ denotes the inferred DF and $f_{\rm i}^{\rm MC}$ denotes the Monte Carlo DF on the ith grid point.

We have performed two types of Monte Carlo tests. In the first, we place the artificial data points exactly on the predicted kinematic profiles of the Monte Carlo model, but use the error bars from the observations. In this case, the rms deviation of the recovered distribution function from the underlying model DF is 19 per cent. The corresponding deviation in the isotropically averaged DF $\bar{f}$ is only 10 per cent. This is a favourable case without sampling errors.

In the second, more realistic, test the artificial data are drawn from the Monte Carlo model as Gaussian variates with the appropriate observational errors. Fig. 6 shows, for a typical set of Monte Carlo data, both the original DF (dots) and the recovered DF (solid lines) in this case. Again the DF is recovered with good accuracy in the entire energy range. Typical rms errors are 13 and 27 per cent for $\bar{f}$ and f, respectively, as determined from 10 different Monte Carlo samples. Note that at the very centre the DF is only constrained by the intrinsic density, as the kinematic data trace the DF only outside a minimal radius. Therefore it is not possible to determine the anisotropy in the very centre, and this point has been excluded in the computation of the quoted χ^2 values.

5 THE DYNAMICS OF NGC 1600

Figs 7–9 show the results of applying our method to the boxy elliptical galaxy NGC 1600. The program was asked to fit the edge-on deprojected density distribution, and the minor and major axis velocity dispersions and line-profile shape parameters h_4 from Bender et al. (1994). Fig. 7 shows these data and the best-fitting three-integral model, as well as, for comparison, the best-fitting two-integral model. It is clear that NGC 1600 requires a three-integral DF. The two-integral model is a very poor fit to the kinematic data, consistent with previous similar but weaker results based on only velocity dispersions (van der Marel 1991, 1998). For the three-integral model, the rms relative deviation of the density is $\approx$1.1 per cent, and the fit of the kinematic data is within one standard deviation in the mean. There are still slight systematic differences between our model of NGC 1600 and the kinematic data on the minor axis. If these are confirmed with higher signal-to-noise data, this might require an inclination angle less than 90° or possibly a slightly triaxial potential.

These plots involve scaling the model DF to the data; the scaling constant gives the mass-to-light ratio. This was found by finding the best-fitting three-integral model for a range of values

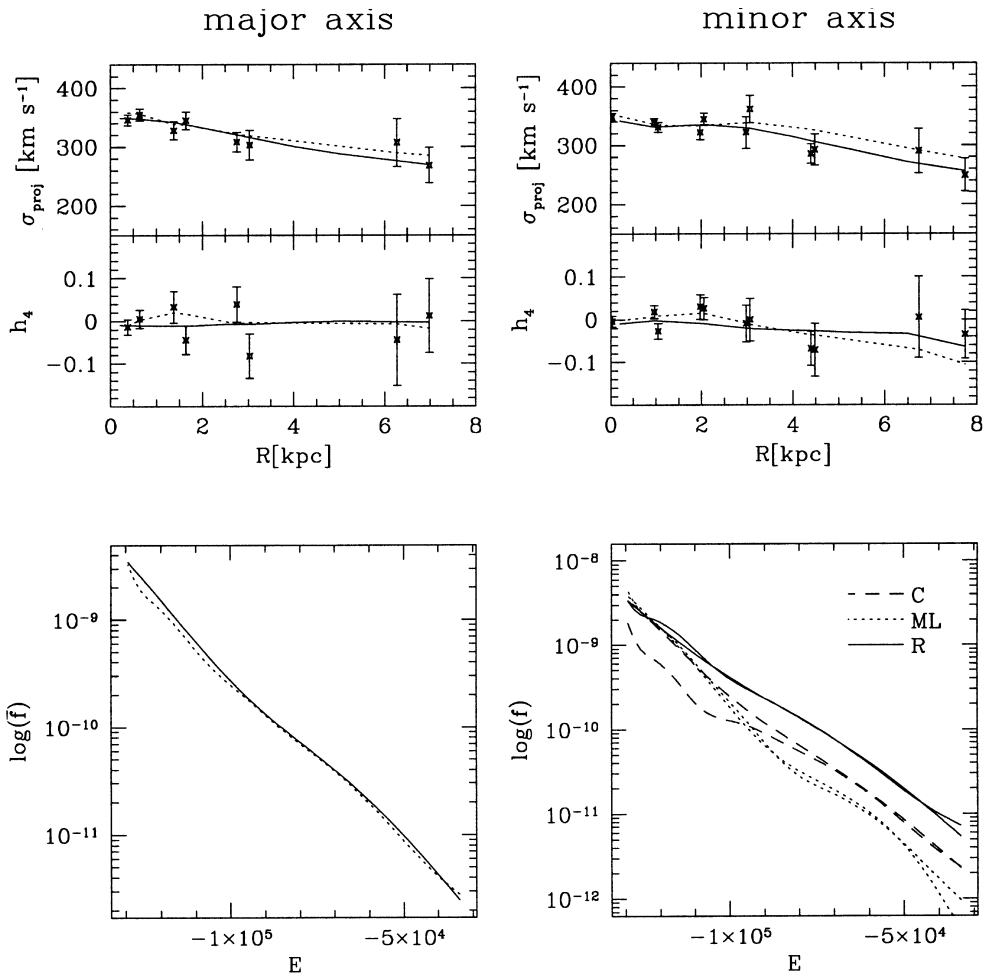

Figure 6. Applying the method to one of the Monte Carlo data sets. First row: projected kinematics for major (left) and minor axis (right). The solid lines represent the input model, the dotted lines show the kinematics of the model recovered from the artificial data (points with error bars). Second row: in the left panel, the averaged distribution function $\bar{f}(E)$ is shown for input model (solid line) and recovered model (dotted line) as a function of energy. The right panel shows the values of the DF for three typical orbits near the radial, meridional loop and circular orbits, again as functions of energy. Each line type corresponds to one of these orbits, showing both the input and the recovered distribution function. In this example, the rms errors of $\bar{f}$ and f are 13 and 27 per cent, respectively.

of the scaling constant, and then determining the optimal value: we thus obtain a best $M/L_V = 6$ and the model shown in Fig. 7. Even for models that do not fit the kinematic data well, we have always found M/L_V in the range 5.5–6.8.

A sample of the implied phase-space distribution is given in Fig. 8. Each panel shows a cut through phase space at a fixed energy, with corresponding circular orbit radius given in the caption. On each energy surface, f is given as a function of the angular momentum scaled to the maximal value possible at that energy and the third integral K similarly scaled. The vertical surfaces limit the part of integral space accessible to stars at this energy. Each corner of this triangular structure represents a special orbit: e.g. the circular orbit with the highest angular momentum is located towards the front of the surface, and the radial orbit in the equatorial plane is located at the top right corner. The left boundary represents the shell orbits, the boundary to the right the equatorial orbits. See also Section 4.3.

From Fig. 8 one sees that in the outer parts of the galaxy (upper row) the radial orbits dominate. By contrast, the central regions of the galaxy (lower row) are more isotropic, although some radial anisotropy is still present. In the very centre (lower right panel for circular orbit radii of ≈0.5 kpc), meridional loop orbits are seen to dominate over equatorial radial orbits. The transition between radii of 0.5–1.5 kpc coincides with the rise of the velocity dispersion that occurs approximately in this range of radii on both axes.

To reaffirm this conclusion Fig. 9 shows the inferred intrinsic velocity dispersions and anisotropy parameters on the true major and minor axes of NGC 1600. On the major axis the radial dispersion σ_r exceeds the azimuthal dispersion σ_ϕ and the meridional dispersion σ_θ; outside the central ∼1.5 kpc the values of the two anisotropy parameters $\beta_\phi \equiv 1 - \sigma_\phi^2/\sigma_r^2$ and $\beta_\theta \equiv 1 - \sigma_\theta^2/\sigma_r^2$ are ∼0.4 and the model is thus radially anisotropic, but approximately isotropic in the (θ,ϕ)-plane. At small radii along the major axis, σ_ϕ increases to $\sim\sigma_r$, while σ_θ remains low.

On the minor axis, σ_r exceeds σ_θ outside $z \simeq 3$ kpc. The inferred radial anisotropy is distinctly less than on the major axis. Moreover, at small radii along the minor axis, the dynamical structure is reversed: there we have $\sigma_\theta > \sigma_r$, with β_θ reaching −0.5 near the centre. The transition between the two regimes corresponds to the change from predominantly equatorial radial orbits and meridional butterfly orbits to predominantly meridional

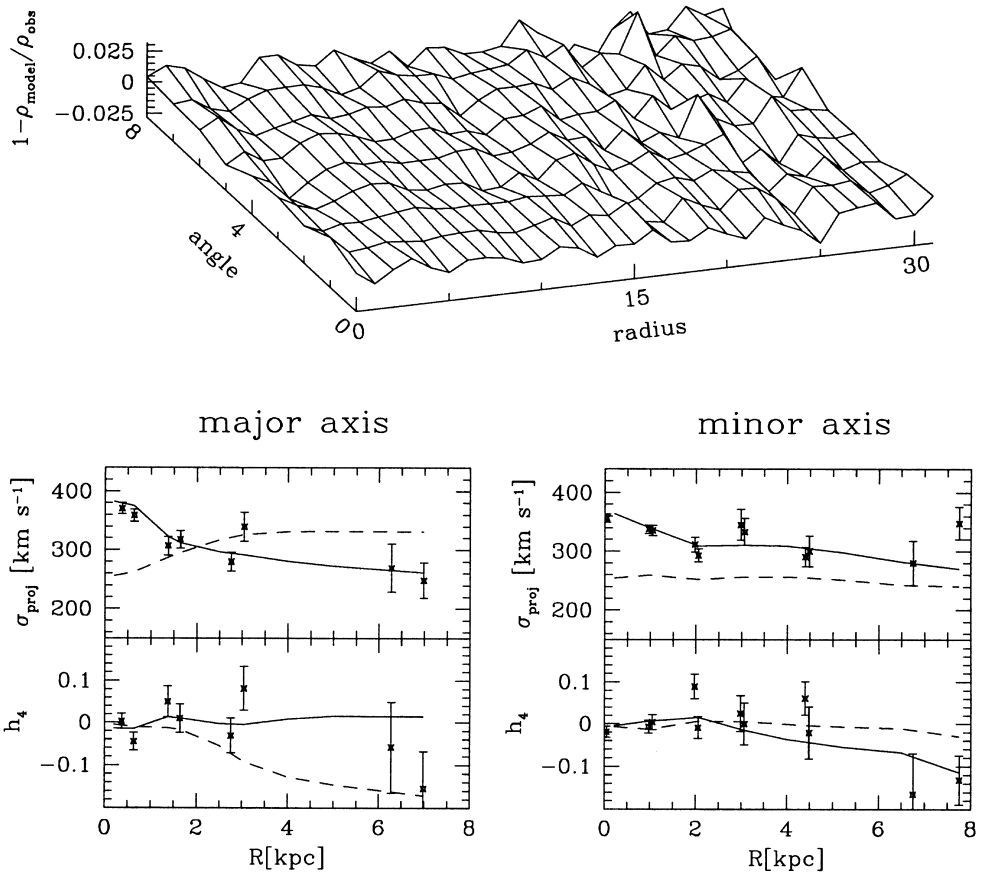

Figure 7. Best-fitting dynamical model for NGC 1600, derived from the deprojected density and the line-profile data of Bender et al. (1994). Top: relative deviation between deprojected and model density. Coordinates are indices of a grid in the meridional plane. The rms relative deviation of the density is 1.1 per cent. Bottom: velocity dispersion and h_4 parameter on the major and minor axes. The best-fitting three-integral model is shown by thick lines; for comparison, a two-integral model $f(E, L_z)$ is also shown (dashed lines).

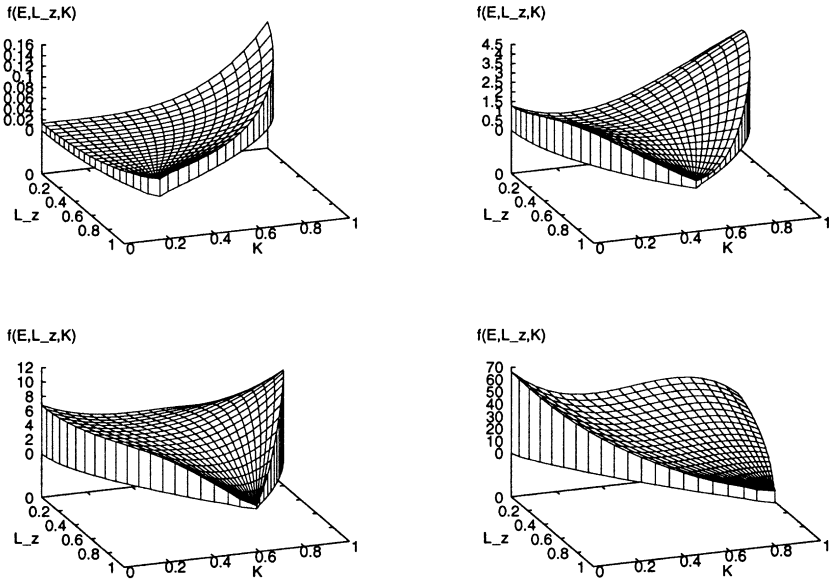

Figure 8. The inferred DF of NGC 1600 at four different energies, parametrizing shells from far out (top left) to near the centre (bottom right). The circular orbit radii corresponding to these energies are $R_c = 16, 2.9, 1.6, 0.5$ kpc. Throughout most of the galaxy, the DF is strongly peaked on the equatorial radial orbit (top right corner in each panel). Inside the core region ($R_b = 1.85$ kpc on the major axis) the model becomes less radially anisotropic.

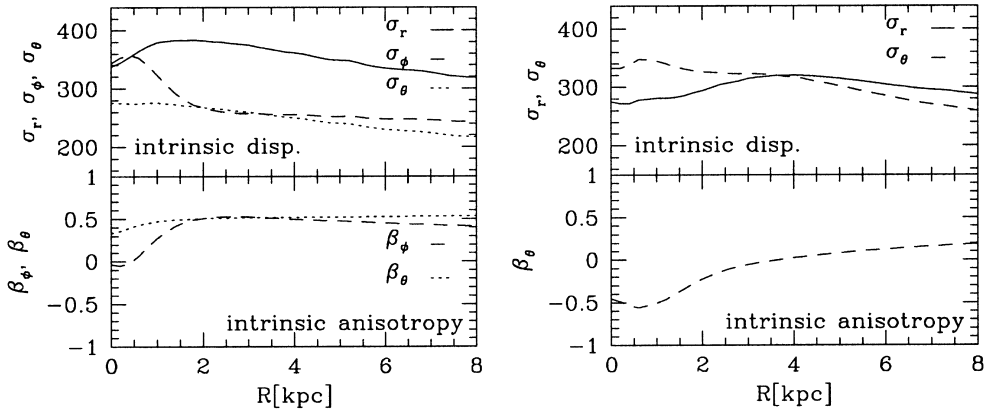

Figure 9. Intrinsic velocity dispersions and anisotropy parameters for NGC 1600. Left: on the R-axis. Right: on the true minor (z-)axis. The anisotropy parameter $\beta = 1 - \sigma_t^2/\sigma_r^2$ is positive for radial anisotropy.

loop orbits, that occurs at circular orbit radii around ∼1 kpc (see Fig. 8). For comparison, the radius marking the edge of the central core region of NGC 1600 is ∼1.85 kpc on the major and ∼1.3 kpc on the minor axis.

In their study of the dynamics of three-integral oblate galaxy models, Dehnen & Gerhard (1993a) identified several ways of constructing a self-consistent, flattened system. Comparing with their results, it appears that the dynamics of NGC 1600 is closest to their models 8 and 9, in which the flattening is achieved by putting extra mass on equatorial radial orbits. This leads to the required excess in the x- and y-kinetic energies compared with the kinetic energy in the z-direction, and to a stronger radial anisotropy on the major than on the minor axis. This pattern is similar to that inferred above for NGC 1600, although the effect is more pronounced in Dehnen & Gerhard's quoted models (their model 8 is isotropic on the minor axis). Compare figs 12 (DF), 17 (velocity ellipsoids) and 18–19 (kinematics) of Dehnen & Gerhard (1993a) and also Fig. 4 of Dehnen & Gerhard (1993b). One characteristic for this orbit structure is that the ratio of the measured velocity dispersions on the minor and major axes is significantly above unity; for NGC 1600, $\sigma_{\rm minor}/\sigma_{\rm major} \simeq 1.15$ at $R = 4$ kpc.

6 CONCLUSIONS AND DISCUSSION

The main result of this study is that the dynamics of NGC 1600 is consistent with a radially anisotropic, axisymmetric three-integral DF, in which the flattening is achieved by putting extra mass on equatorial radial orbits. Two-integral DFs cannot reproduce the kinematic data. The radial anisotropy is strongest in the outer parts of the modelled range (out to $R_{\rm e}/2$), with $\sigma_\theta/\sigma_r \approx \sigma_\phi/\sigma_{\rm r} \approx 0.7$ on the major axis. On the minor axis and near the centre, the galaxy is more isotropic. The inferred mass-to-light ratio is $M/L_V = 6\,h_{50}$ with an uncertainty of $\approx \pm 0.5\,h_{50}$.

Comparing similar ground-based data with the predictions of two-integral models, Magorrian et al. (1998) inferred a central massive object of $M_\bullet \simeq 10^{10}\,{\rm M}_\odot$ in NGC 1600. Our analysis here shows not only that a two-integral model is inconsistent with the measured line-profile shape parameters, but also that the rise of the central velocity dispersion seen in these ground-based data is fitted well with a radially anisotropic three-integral model without a black hole (note, however, that because of the limited radial range of the line-profile data we have used, the contribution of high-energy radial orbits to the central velocity dispersion peak might be overestimated). Given the overall radial anisotropy of NGC 1600, it is likely that the black hole in NGC 1600 has a smaller mass than inferred by Magorrian et al. (1998). The kinematic data used here do not discriminate for or against such smaller black-hole masses; to reduce the ambiguity in the central gravitational potential requires high-resolution data (e.g. Kormendy & Richstone 1995) with small error bars. Using HST data for NGC 3379 and orbit distribution modelling, Gebhardt et al. (1999) indeed found that the implied black-hole mass in their best-fitting model for NGC 3379 is a factor of approximately 6–7 lower than that inferred by Magorrian et al. (1998).

Besides NGC 1600, radial anisotropy has also been inferred in several E0 galaxies for which a line-profile analysis has been done: NGC 2434 (Rix et al. 1997), NGC 6703 (Gerhard et al. 1998), NGC 1399 (Saglia et al. 1999) and NGC 3379 (Gebhardt et al. 1999). The model of Dejonghe et al. (1996) for the flattened elliptical galaxy NGC 4697 has $\sigma_\phi > \sigma_r > \sigma_z$, whereas NGC 1700 appears to be tangentially anisotropic (Statler, Dejonghe & Smecker-Hane 1999); for both of these objects no line-profile data were used, however. Two S0 galaxies (NGC 3115, Emsellem et al. 1999; NGC 4342, Cretton & van den Bosch 1999) have dominant σ_ϕ dispersion. Although the number of galaxies investigated in enough detail is still small, there are the beginnings of a trend in that large ellipticals appear to show a transition from a nearly isotropic central region to a moderately radially anisotropic main body. We are currently applying our technique to several other elliptical galaxies to see whether this trend holds up.

Our method is an adaptation of the techniques of Dehnen & Gerhard (1993a) to axisymmetric galaxy potentials. First, the galaxy is deprojected, and the luminosity density and corresponding potential are determined. From the potential, we calculate an approximate third integral K from perturbation theory (see Gerhard & Saha 1991). We then write the distribution function as a sum over basis functions in the three integrals of motion (E, L_z, K), and fit to the observed velocity moments and line-profile parameters, using a regularized non-parametric technique. The method has been validated by recovering a model distribution function from its 'observable' kinematics. One advantageous feature of our technique is that it directly yields the phase-space distribution function of the galaxy. Its main restriction is to potentials in which the third integral gives a good approximation to the orbital tori and, if stochastic regions are present, to their boundaries. In this way, stochastic orbit building blocks can be constructed. In the deprojected axisymmetric potential of NGC

1600, stochastic orbits are unimportant and resonant orbit families take up only a minor fraction of phase space; for this galaxy, the perturbation integral gives an excellent fit to most orbits (Fig. 2).

We now discuss our results in the light of a possible merger origin for elliptical galaxies. Because of the very large number of relevant parameters, no specific large-N merger-remnant model to match a particular galaxy will be available for some time. By comparing in qualitative terms the main aspects of the dynamical structure inferred for NGC 1600 with the dynamics of those merger remnants that have been analysed, we may none the less gain some insight into the kind of merger process that may have shaped this galaxy.

The dynamical properties of the remnants in the published merger calculations depend strongly on the assumed physics and initial conditions. Mergers between two purely stellar, about-equal-mass disc galaxies typically result in remnants with large triaxiality and kinematic misalignment (Barnes 1992; Heyl, Hernquist & Spergel 1996), unless the encounter is a prograde one with relatively large impact parameter. Remnants of minor mergers rotate significantly (Barnes 1998). Including a gaseous component in the simulations, even with only a small fraction of the total mass, results in significantly more oblate remnants and in a smaller fraction of box orbits relative to tube orbits; however, the difference in orbital structure due to different numerical algorithms is substantial (fig. 17 of Barnes & Hernquist 1996).

Another possible process is the merging of several smaller parts to one large galaxy (Weil & Hernquist 1996; Dubinski 1998). Again, the initial trajectories of the merging galaxies have an important impact on the remnant. The remnants resulting from nearly isotropic initial conditions are clearly more axisymmetric and rounder than pair-merger remnants, but show large rotation velocities (Weil & Hernquist 1996). Dubinski (1998) used CDM simulations to get initial conditions at $z = 2$. From that time on, he followed the merging process to a brightest cluster galaxy. In his simulation, merging pieces fall in mainly along filaments. The resulting remnant has a triaxial shape aligned with its environment, it shows only slow rotation around the small axis, and is mildly radially anisotropic with anisotropy parameter increasing slowly outwards.

The lack of rotation in NGC 1600 clearly argues against a binary merger on a wide orbit or a merger of a near-isotropic galaxy group as simulated by Weil & Hernquist (1996). We do not know how strongly triaxial NGC 1600 is (the argument given in the Introduction is statistical, and the kinematic misalignment in this galaxy is not well defined). However, our derived DF for NGC 1600 (Fig. 8) has a strong bias towards radial (z-tube) orbits. By contrast, the angular momentum distributions for the *z-tube orbits* alone in the merger remnants analysed by Barnes (1992) and Barnes & Hernquist (1996) are fairly uniform. The inferred large extra mass on radial orbits in NGC 1600 may then either correspond to the large fraction of box orbits present in some of these remnants (if NGC 1600 is significantly triaxial), or it may have evolved out of such box orbits if the shape of NGC 1600 has evolved towards axisymmetry since its formation. In either case, the large radial orbit fraction argues for a merger in which the effects of gas were not very important. This argument is also supported by the large observed core radius of NGC 1600. Thus the dynamics of NGC 1600 appear consistent both with a mainly collisionless, low-angular momentum binary merger and with a variant of the merging along filaments described by Dubinski (1998).

It will be interesting to address such questions for several more elliptical galaxies, hopefully with a larger sample of quantitatively analysed merger remnants at hand. In our view, for these comparisons the most helpful structural information about the merger remnants will be their three-dimensional velocity ellipsoids.

ACKNOWLEDGMENTS

We thank Ralf Bender for sending us his unpublished surface photometry, Walter Dehnen for the use of his programs, David Merritt for a discussion about regularization techniques, and the referee Tim de Zeeuw for comments that improved the presentation of this paper. We gratefully acknowledge support by the Swiss National Fund under Grants 20-43218.95 and 20-50676.97.

REFERENCES

Barnes J. E., 1992, ApJ, 393, 484
Barnes J. E., 1998, in Kennicutt R. C., Schweizer F., Barnes J. E., eds, Galaxies: Interactions and Induced Star Formation, Saas-Fee Adv. Course 26. Springer, Berlin
Barnes J., Hernquist L., 1996, ApJ, 471, 115
Bender R., Saglia R. P., Gerhard O. E., 1994, MNRAS, 269, 785
Binney J. J., Tremaine S., 1987, Galactic Dynamics. Princeton University Press
Binney J. J., Davies R., Illingworth G., 1990, ApJ, 361, 78
Cretton N., de Zeeuw P. T., van der Marel R. P., Rix H.-W., 1999, ApJ, submitted (astro-ph 9902034)
Cretton N., van den Bosch F. C., 1999, ApJ, 514, 704
Dehnen W., 1995, MNRAS, 274, 919
Dehnen W., Gerhard O. E., 1993a, MNRAS, 261, 311
Dehnen W., Gerhard O. E., 1993b, in Danziger I. J., Zeilinger W. W., Kjär K., eds, Structure, Dynamics and Chemical Evolution of Early-type Galaxies. ESO, Garching, p. 327
Dejonghe H., de Bruyne V., Vauterin P., Zeilinger W. W., 1996, A&A, 306, 363
Dubinski J., 1998, ApJ, 502, 141
Emsellem E., Dejonghe H., Bacon R., 1999, MNRAS, 303, 495
Faber S. et al., 1997, AJ, 114, 1771
Franx M., Illingworth G., de Zeeuw T., 1991, ApJ, 383, 112
Gebhardt K. et al., 1996, AJ, 112, 105
Gebhardt K. et al., 1999, preprint
Gerhard O. E., Binney J. J., 1985, MNRAS, 216, 467
Gerhard O. E., Binney J. J., 1996, MNRAS, 279, 993
Gerhard O. E., Saha P., 1991, MNRAS, 251, 449
Gerhard O. E., Jeske G., Saglia R. P., Bender R., 1998, MNRAS, 295, 197
Hanson R. J., Haskell K.vH., 1981, Math. Program., 21, 98
Heyl J. S., Herquist L., Spergel D. N., 1996, ApJ, 463, 69
Hunter C., de Zeeuw T., 1992, ApJ, 389, 79
Jedrzejewski R., Schechter P. L., 1989, AJ, 98, 147
Kormendy J., Bender R., 1996, ApJ, 464, 119
Kormendy J., Richstone D., 1995, ARAA, 33, 581
Lucy L., 1974, AJ, 79, 745
Magorrian J. et al., 1998, AJ, 115, 2285
Merritt D., 1993, in Danziger I. J., Zeilinger W. W., Kjär K., eds, Structure, Dynamics and Chemical Evolution of Early-type Galaxies. ESO, Garching, p. 275
Merritt D., Fridman T., 1996, ApJ, 460, 136
Merritt D., Quinlan G. D., 1998, ApJ, 498, 625
Merritt D., Tremblay B., 1994, AJ, 108, 514
Richstone D. et al., 1998, Nat, 395, A14
Rix H. W., de Zeeuw P. T., Cretton N., van der Marel R. P., Carrollo C. M., 1997, ApJ, 488, 702
Saglia R. P., Kronawitter A., Gerhard O. E., Bender R., 1999, AJ, submitted

Schwarzschild M., 1979, ApJ, 232, 236
Scott D. W., 1992, Multivariate Density Estimation. Wiley
Statler T. S., Dejonghe H., Smecker-Hane T., 1999, ApJ, 117, 126
Tremblay B., Merritt D., 1996, AJ, 111, 2243
van der Marel R., 1991, MNRAS, 253, 710
van der Marel R., 1998, in Sanders D. B., Barnes J., eds, Galaxy Interactions at Low and High Redshift. Kluwer, Dordrecht
van der Marel R., Sanders D. B., Barnes J., 1998, Galaxy Interactions at Low and High Redshift. Kluwer, Dordrecht, in press
van der Marel R., Cretton N., de Zeeuw P. T., Rix H. W., 1998, ApJ, 493, 613
Wahba G., Wendelberger J., 1980, Monthly Weather Rev., 108, 1122
Weil M., Hernquist L., 1996, ApJ, 457, 51

This paper has been typeset from a TEX/LATEX file prepared by the author.